metals

MDPI

Article

The Identification of a New Liquid Metal Embrittlement (LME) Type in Resistance Spot Welding of Advanced High−Strength Steels on Reduced Flange Widths

Keke Yang [1], Gerson Meschut [1], Georg Seitz [2,*], Max Biegler [2] and Michael Rethmeier [4,2,3]

[1] Laboratory for Material and Joining Technology (LWF), 33098 Paderborn, Germany; keke.yang@lwf.uni-paderborn.de (K.Y.); meschut@lwf.uni-paderborn.de (G.M.)
[2] Fraunhofer Institute for Production Systems and Design Technology (IPK), 10587 Berlin, Germany; max.biegler@ipk.fraunhofer.de (M.B.); michael.rethmeier@ipk.fraunhofer.de (M.R.)
[3] Federal Institute for Materials Research and Testing (BAM), 12205 Berlin, Germany
[4] Institute for Machine Tools and Factory Management (IWF), Technical University of Berlin, 10623 Berlin, Germany
* Correspondence: georg.seitz@ipk.fraunhofer.de; Tel.: +49-30-39006-218

Abstract: Liquid metal embrittlement (LME) cracking is a phenomenon observed during resistance spot welding (RSW) of zinc−coated advanced high−strength steels (AHSS) in automotive manufacturing. In this study, severe cracks are observed at the edge of the sheet under reduced flange widths. These cracks, traversing the AHSS sheet, culminate at the edge with a width of approximately 1.2 mm. Through combined numerical and experimental investigations, and material testing, these cracks are identified and validated as a new type of LME crack. The mechanism behind this crack formation is attributed to unique geometric conditions that, when compared to center welding, amplify radial material flow by ninefold to 0.87 mm. The resultant tangential tensile stresses approximate 760 MPa, which exceed the yield strength of the examined advanced high−strength steel (AHSS) under heightened temperature conditions, and when combined with liquid zinc, promote the formation of this new type of LME crack.

Keywords: Liquid metal embrittlement; crack; advanced high strength steels; resistance spot welding; simulation; flange width

Citation: Yang, K.; Meschut, G.; Seitz, G.; Biegler, M.; Rethmeier, M. The Identification of a New Liquid Metal Embrittlement (LME) Type in Resistance Spot Welding of Advanced High−Strength Steels on Reduced Flange Widths. *Metals* **2023**, *13*, 1754. https://doi.org/10.3390/met13101754

Academic Editors: Christopher DiGiovanni and Ali Ghatei-Kalashami

Received: 11 September 2023
Revised: 7 October 2023
Accepted: 10 October 2023
Published: 16 October 2023

1. Introduction

Automobile manufacturers prioritize lightweight designs to augment driving safety and concurrently reduce emissions [1]. Advanced High−Strength Steels (AHSS) are favored for their optimal balance between elongation and tensile strength, aligning with these objectives [2]. Zinc coating is utilized as an effective anti−corrosion technique for advanced high−strength steels (AHSS) [3]. However, during high−temperature manufacturing processes, especially when the processing temperature exceeds the melting point of zinc (420 °C), such as hot press forming and resistance spot welding (RSW), steel with zinc coatings becomes susceptible to liquid metal embrittlement (LME) [4]. A particular concern is 'zinc−assisted LME', where liquid zinc penetrates the steel substrate via the grain boundaries of a vulnerable microstructure, facilitated by tensile stress. This leads to grain boundary decohesion and eventual cracking in the steel [5].

In the fabrication of body−in−white (BIW) components, RSW is the preferred method for joining these steel types [6]. Therefore, the feasibility of joining galvanized AHSS through RSW determines whether they can be successfully incorporated into automotive manufacturing [7]. Ashiri et al. [8] pointed out that, compared to conventional steels, the richer chemical composition and higher strength of AHSS make them more susceptible to LME. Furthermore, Bhattacharya elaborated on the fundamental conditions for LME occurrence, emphasizing that materials become susceptible to LME when specific loads or

stresses and liquid zinc are present simultaneously [9]. Hot tensile tests determined the critical temperature conditions for LME, revealing that temperatures between 700 °C and 900 °C led to increased LME susceptibility [10]. Nicholas and Old underscored the role of stress, noting that sheet materials must experience sufficient stress levels to induce minor plastic deformations [11]. Echoing this, DiGiovanni et al. reported that increasing stress levels by applying external loads heightens brittleness to LME [12]. Modern finite element analyses by Jung have shown that tensile stresses generated during the RSW cooling phase surpass the yield strength, highlighting the clear risk of LME in AHSS [13]. Currently, beyond examining steel substrates and stress, El−Sari et al. have investigated the effect of different AHSS coatings on LME sensitivity. They found that zinc–magnesium coatings (ZM) had the most substantial influence, followed by galvanized (GI) and galvannealed (GA). Electrogalvanized (EG) coatings exhibited the least sensitivity to LME [14].

Several studies have explored methods to mitigate LME cracks. DiGiovanni et al. demonstrated that by utilizing a ramp−down welding current during RSW, the severity of LME can be mitigated [15]. Song et al. discovered that varying electrode forces can similarly reduce the occurrence of LME [16]. Delving deeper into the RSW process, Lalachan et al. [17] pinpointed that escalating the growth rate of electrode cap contact with the sheet can mitigate LME cracks. Outside of process adjustments, Böhne et al. highlighted that broadening the working diameter of the electrode cap stands as an effective strategy against LME [18]. On the materials front, Van der Aa et al. evaluated how high−temperature cycling could modify the microstructure of zinc−coated AHSS to resist LME [19]. Similarly, Kim et al. showcased the potential of an α−Fe(Zn)−layer in hindering liquid zinc from contacting the steel substrate, thereby reducing LME risks [20]. Ghatei−Kalashami et al. reinforced this observation, noting that sustained, high−intensity tensile stress has the potential to fracture the α−Fe(Zn,Al)−layer, thereby exacerbating the formation of LME cracks [21]. Shifting the focus to zinc's intrinsic effects, Wang et al. [22] conducted hot tensile tests on both zinc−coated and uncoated steels. Their findings revealed a notable reduction in plastic deformation for zinc−coated samples, emphasizing the embrittling influence of liquid zinc.

To ensure the weldability of AHSS components, these parts are designed with broad flanges. Typically, these range from 16–20 mm in width. This design choice leads to increased material usage and consequently, added weight to the overall vehicle structure. Given this, there is a growing emphasis, especially in mass−market steel car bodies, on reducing the flange width of components to less than 10–12 mm as a weight−reduction measure. However, with reduced flange widths, there is a risk that spot welds might be dangerously close to the sheet's edge, often due to common assembly positioning errors in production. Thus, a pivotal requirement for realizing these weight−saving benefits is the capacity to consistently and safely employ effective joining techniques at these reduced flange widths. Achieving this without compromising joint strength or excessively increasing the number of spot welds is paramount. This situation underscores a pressing research imperative in joining technology, with a particular focus on RSW given its widespread use in automotive body manufacturing [23].

Manzenreiter et al. investigated the influence of the distance between spot welds and the edges of components on galvanized hot−stamped steel [24]. Their results indicated that when this distance is reduced below a certain threshold, cracking occurs near the edge. Owing to the notch effect, these observed cracks cause the component to fail under lower energy levels during load−bearing assessments. Regrettably, the study did not provide comprehensive photographic documentation of these cracks, nor did it elucidate or pinpoint their causative factors. As a result, the precise mechanism triggering these cracks remains ambiguous.

In response to the aforementioned research gap, the study first identifies the pivotal flange width at which crack initiation is observed. Employing the hypothetico−deductive method, it is proposed that such cracks could be categorized as LME cracks. To validate this hypothesis, an integrative approach is adopted, merging experimental research, material

testing, and finite element simulations, aiming to determine if these cracks conform to the recognized conditions for LME occurrence. Subsequently, a detailed analysis of crack formation is undertaken, exploring the inherent mechanisms involved. In conclusion, the distinct attributes of these cracks are characterized and detailed.

2. Novelty and Application

Driven by the automotive manufacturing industry's shift towards reduced flange widths for lightweight designs, this research identifies significant cracking at the sheet edge attributed to such reductions. Merging insights from experimental validation and numerical simulations, the findings confirm that these observed cracks align with the prerequisites for LME crack formation. The observed brittle fracture cross−section combined with the penetration of liquid zinc into the steel substrate, designated this as a new type of LME crack. Unlike conventional LME cracks, which are primarily confined to the electrode indentation in a ring−like configuration [25], this newly identified type of LME crack is evident outside the electrode indentation, presenting as an inverted cone that traverses the AHSS material.

This research emphasizes a critical knowledge gap in LME crack behavior due to reduced flange widths and underscores the need to refine RSW techniques for compatibility. By defining this new type of LME crack, a fresh framework for scrutinizing LME cracks within RSW is established. By uncovering the origins of this particular crack type, the study broadens understanding of LME behaviors in RSW and charts a course for the development of mitigation strategies in subsequent applications.

3. Materials and Methods

The experiments detailed in this article employ a dual−phase (DP) steel that is electro−galvanized (EG) on both surfaces and belongs to a strength class of 1200 MPa. This material is denoted as DP1200 DH, aligning with CR850Y1180T−DH as referenced in [26], and serves as the representative AHSS material [27]. Distinctively, the DP1200 DH, a third−generation AHSS, exhibits superior ductility compared to conventional DP steels within the same strength bracket. For this research, DP1200 DH is paired with a hot−dip galvanized (DHG) mild steel (DX56D) [28]. Tables 1 and 2 outline the chemical composition and mechanical attributes of the materials respectively. The choice of this material pairing draws inspiration from the insights of Benlatreche et al., aligning with contemporary industrial interests [29]. In the experimental setup, the DP1200 DH sheet is placed on the anodic side, while the mild steel sheet is on the cathodic side.

Table 1. Chemical composition of the utilized material combination determined by heat analysis (expressed in weight−%) [27,28].

	C	Si	Mn	P	Al	Cr + Mo	Ti	B	Cu
DP1200 DH	0.23	2.00	2.9	0.05	0.015–2.0	1.40	0.15	0.005	0.20
DX56D	0.12	0.50	0.6	0.10	–	–	0.30	–	–

Table 2. Mechanical properties of the utilized material combination determined by tensile test [27,28].

	Thickness [mm]	0.2% Yield Strength $R_{p0.2}$ [MPa]	Tensile Strength R_m min. [MPa]	Total Elongation A_{80} min. [%]
DP1200 DH	1.51	850–1050	1180–1350	13
DX56D	2.00	120–180	260–350	39

The experiments utilized a 1000 Hz medium frequency direct current (DC) in RSW, executed with a pedestal servo−electric x−type welding gun depicted in Figure 1. The electrodes were water−cooled at a rate of 4 l/min, and the electrode cap conformed to the

F1−16−20−50−5.5 specifications as outlined in ISO 5821 [30]. The welding current range was set according to prevalent industry standards [31]. For this study, assessments were conducted on test specimens measuring 45 × 45 mm^2.

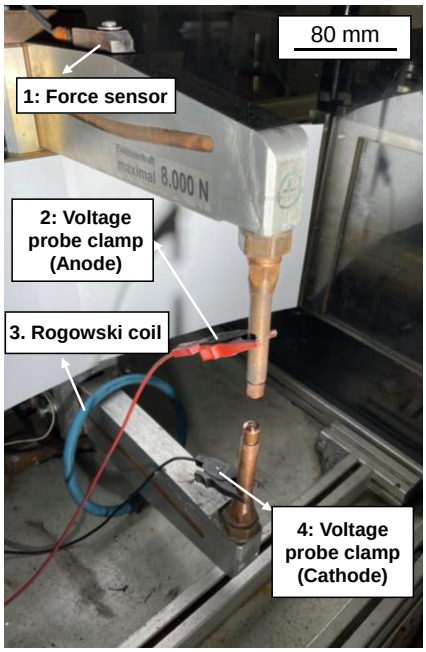

Figure 1. Experimental setup with multiple measurement devices and sensors.

Table 3 presents the welding parameters. A comparative analysis of spot welds at four distinct edge distances is conducted. Here, the edge distance is defined as the distance from the center of the electrode cap to the sheet edge. The electrode force, welding time, squeeze, and holding time parameters are selected based on [31]. The welding current used at different edge distances corresponds to the maximum spatter−free welding current determined at the sample center. Surface views of the spot welds were analyzed for a comparative evaluation.

Table 3. Welding Parameters.

Electrode Geometry	F1−16−20−50−5.5
Electrode force	4.5 kN
Weld current	9.5 kA
Weld time	380 ms
Squeeze/Hold time	300 ms
Edge distance	4 mm, 5 mm, 6 mm, 7 mm
Stack−ups	DP1200 DH/mild steel

To examine the zinc coating's influence on the crack, this study used both galvanized and non−galvanized steel sheets with the identical welding parameters. For the preparation of non−galvanized steel sheets, the zinc coating was removed using a 20% hydrochloric acid solution. A visual inspection of the sheets was subsequently performed using an optical microscope, with findings documented photographically. The sample was cross−sectioned along any visible cracks, and a Scanning Electron Microscope (SEM) was used to observe the crack's cross−section, helping determine its fracture characteristics. Further analysis was carried out using an Energy Dispersive X−ray Spectrometer (EDX) to ascertain the crack surface's chemical composition, ultimately confirming whether the observed crack was indeed an LME crack.

A rigorous validation of the conditions necessary for LME crack occurrence was achieved using a finite element model developed in Simufact Welding software version

2020.0.1, as cited in [32]. Cross−sectional and transient temperature measurements, in line with [33], validated this model using data from the conducted experiments. The DP1000 material dataset, previously validated in [32], was also utilized, adjusted to match the required $R_{p0.2}$ and R_m values. The contact resistance applied in the simulation model is derived from measurements taken on the material stack−up.

The modeled sheets were geometrically consistent with the actual 45 × 45 mm^2 specimens. Fixed elements at the sheet peripheries were chosen as boundary conditions in the simulation to match the experimental welding configuration. Two distinct models were introduced: one representing a weld at the center of a sheet stack and the other simulating an edge distance of 4 mm (subsequently referred to as "edge welding" within the simulation framework). These models comprised approximately 19,000 linear hexahedral elements, with local refinement zones concentrated in the welding region. In the welding zone, element edge lengths were reduced to as little as 0.26 mm. The computation duration for these intricate, time−dependent, electro−thermomechanical simulations averaged about 1 h and 15 min.

A twofold refinement in the mesh convergence assessment reduced element lengths to 0.13 mm, resulting in a 4% variation in peak process temperature. However, this refinement increased computation times eightfold. A study using a threefold refinement was not pursued due to the excessive computation durations. Given the negligible accuracy variation between the base model and its first refinement, the single refinement model was deemed the most appropriate.

Tangential stresses were extracted from the DP1200 DH sheet's upper surface, specifically at a 4 mm distance from the weld center, and were sourced directly from the outermost edge fiber, which corresponds to the same distance from the weld center.

4. Results and Discussion

4.1. Experimental Identification

Figure 2 displays both top and 45° angled views of spot welds over various edge distances. As the edge distance decreases, there is a notable heat accumulation and significant bulging deformation visible at the steel sheet edge, as seen in Figure 2B,C. As shown in Figure 2D, a longitudinal crack became evident when the edge distance is further reduced to 4 mm. Consequently, an edge distance of 4 mm was chosen for further experimental investigation in this research.

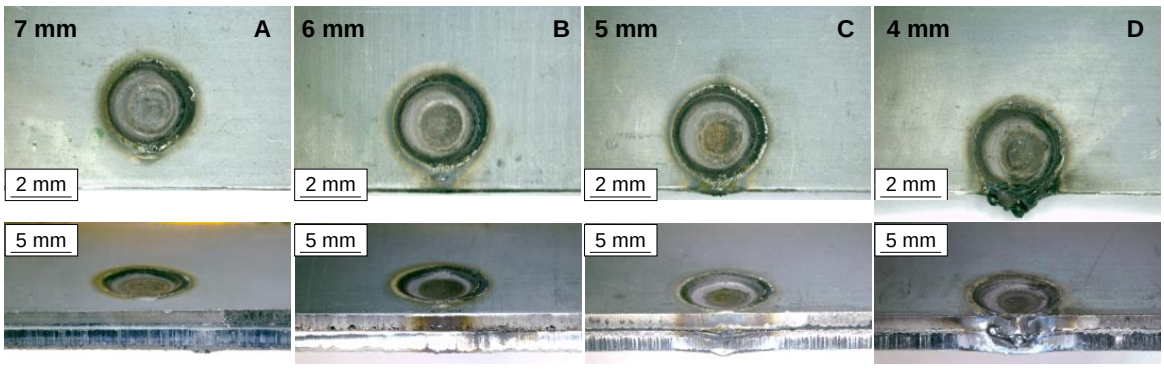

Figure 2. Comparison of solder joint shapes at different edge distances. (**A**): Edge distance is 7 mm. (**B**): Edge distance is 6 mm. (**C**): Edge distance is 5 mm. (**D**): Edge distance is 4 mm.

Figure 3 documents a magnified image of the observed crack, obtained through macroscopic observation, at a 4 mm edge distance. The crack, displaying an inverted cone−shape, is located outside of the electrode's indentation and is widest at the flange edge, approximately 1.2 mm. Additionally, the crack permeates the AHSS material, DP1200 DH, leading to its complete failure at the sheet edge.

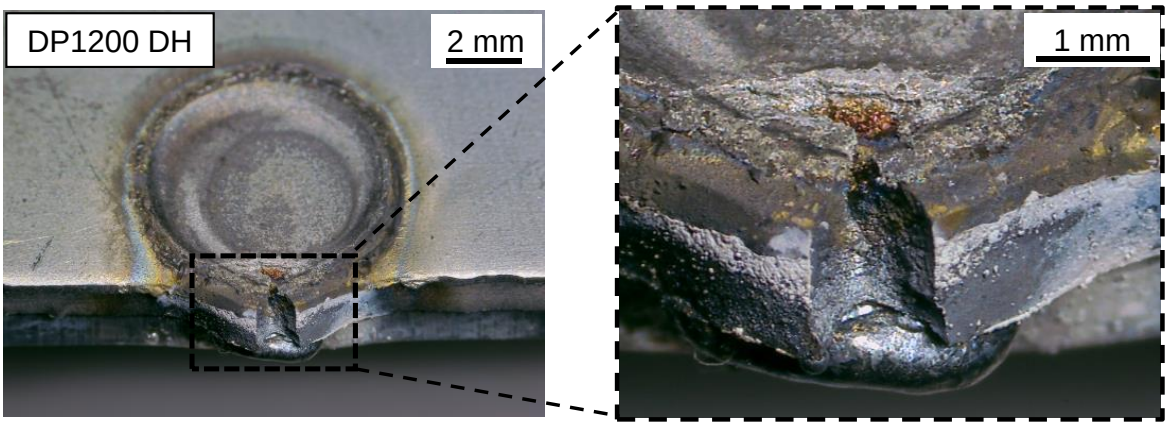

Figure 3. Observation of crack morphology at an edge distance of 4 mm.

The primary task for accurately identifying this type of LME crack is to determine whether the cracking location experiences tensile stress during RSW. This is initially evaluated by observing the deformation (bulging) on the sheet edge. As welding approaches the sheet edge, less solid metal resists the electrode force, leading to plastic deformation and the formation of a bulge. When imagining the outermost fiber during this bulging it can be assumed that because of the 'stretching' of the fiber, tensile stresses are present. This assumption is validated by the numerical simulation shown in Figure 4, taken just before the sheet edge starts to deform. The maximum tensile stress is observed near the sheet's edge. Hence, it is concluded that these cracks satisfy one of the prerequisites for LME occurrence, which is the presence of tensile stress.

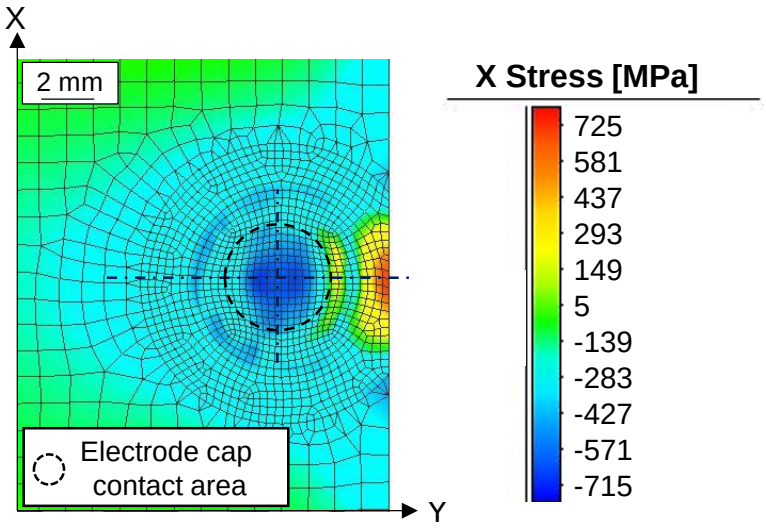

Figure 4. Top view of the peak tensile stress distribution in the X direction on the AHSS side (DP1200 DH) during the welding process at 140 ms.

Having confirmed the existence of tensile stresses at the crack locations, it is important to note that the cracks in this study differ significantly in position and form from traditional LME cracks. To gain a deeper understanding, this study evaluates whether these cracks also meet another LME prerequisite: the influence of liquid zinc on their formation. This was achieved by conducting 20 repeated welding experiments on identical materials with and without zinc coating, using the same welding parameters. The zinc−free samples were obtained by removing the zinc coating with 20% hydrochloric acid. Figure 5 presents a comparative analysis of test results at the 4 mm edge distance, revealing severe cracking in the zinc−coated steel sheets. In contrast, samples devoid of the zinc coating displayed no

evident cracks. These findings indicate that the presence of liquid zinc, rather than tensile stresses, plays a more pivotal role in this crack formation.

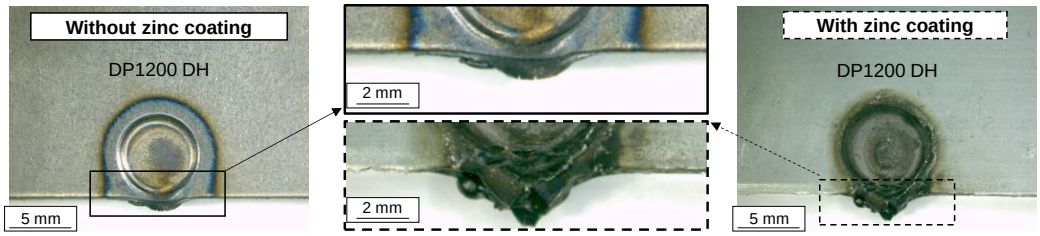

Figure 5. Experimental investigation on the influence of zinc coating on crack formation.

To gain deeper insight into the crack's fracture mechanism, the fracture surface was examined using a Scanning Electron Microscope (SEM), as shown in Figure 6. This examination revealed defining features of a brittle fracture: the surface was luminous, smooth, and consistent, contrasting starkly with the uneven or elongated appearance typical of ductile fractures. Upon magnification, the image revealed numerous "groove−like" patterns, suggestive of swift crack progression during the brittle fracture process. Additionally, the absence of discernible plastic deformation or necking on this surface further attested to its brittle nature.

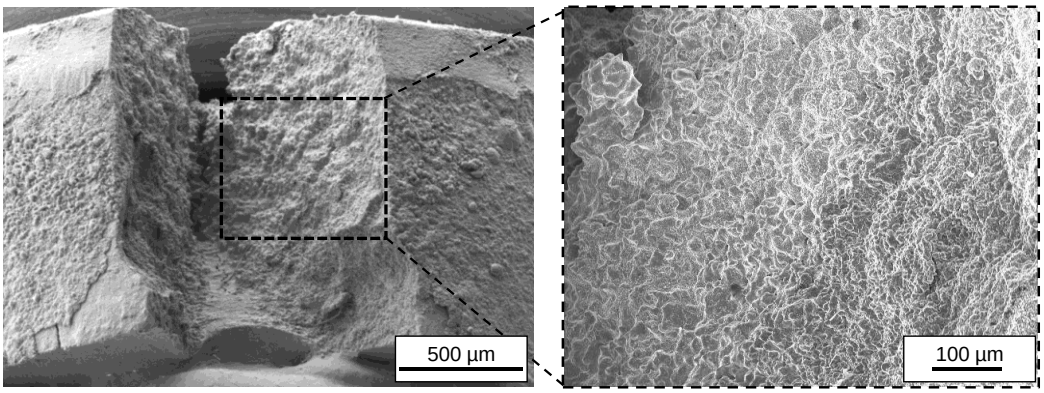

Figure 6. Verification of brittle fracture characteristics of the crack surface through Scanning Electron Microscope (SEM) analysis.

From the preceding analysis, the zinc coating has been identified as the principal factor leading to the brittle fracture of the crack. To delve deeper into the role of this zinc coating in crack formation, this study utilized Energy Dispersive X−ray (EDX) analysis to examine the chemical composition of the fracture surface. The objective was to discern the distribution of chemical elements on this fractured area, and subsequently ascertain if liquid zinc had penetrated into the steel substrate during the welding process. This would determine if the crack's formation was influenced by an LME−mechanism.

As shown in Figure 7a, the sample was specifically processed to ensure a perpendicular scan to the cross−section, aiming to avoid interference from the crack angle during the EDX analysis. To achieve this, a metallographic cutter was used to cut the sample 0.5 mm to the right of the crack's center. This ensured that the left side of the crack, observed subsequently, remained undamaged during the cut, preserving the accuracy of the EDX analysis. As shown in Figure 7b, the crack cross−section is clearly visible behind the cutting surface, confirming that it did not incur any additional damage throughout the preparation process.

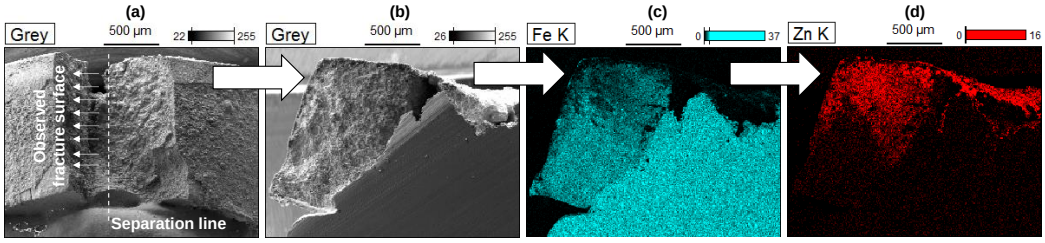

Figure 7. EDX analysis of the penetration of liquid zinc in DP1200 DH during the RSW process. (**a**) Illustration of the sample's cutting direction and observation surface. (**b**) Prepared sample post−processing. (**c**) Distribution of Fe element. (**d**) Distribution of Zn element.

The EDX analysis results clearly indicate the distribution of the Fe element across the sample's cross−section, including both the steel substrate and the crack fracture surface, as shown in Figure 7c. In contrast, the Zn element is only observed on the crack fracture surface, as depicted in Figure 7d. It is important to note the significant non−uniformity in the distribution of the Zn element on the fracture surface. In a vertical orientation, a heightened concentration of the Zn element is evident towards the upper−middle section of the material, proximate to the electrode cap side. This observation supports the assumption that the zinc coating, located near the electrode cap, melted during the welding process. This molten zinc then penetrated the steel substrate, leading to its embrittlement. Under the influence of the previously mentioned tensile stresses acting along the sheet edge, this embrittlement ultimately led to this crack formation.

4.2. Finite Element Simulation

The experimental investigation confirmed that the observed crack in the iron−zinc system meets the essential criteria for LME occurrence. These experimental findings, along with a quantitative analysis of the crack's formation mechanism, will be further validated in subsequent welding simulation investigations.

Employing the same methodology as in the experimental analysis, the deformation at sheet edges is initially quantitatively examined using finite element analysis. This evaluates the local displacement in the Y−direction at the conclusion of the welding process, providing insight into material flow dynamics. To ensure a consistent comparison of ensuing results, designated analysis points (represented by circles) are situated 4 mm from the welding center in both welding scenarios. These findings are depicted in Figure 8. In center welding, there is minimal displacement, peaking at 0.11 mm. Conversely, edge welding registers a considerably elevated maximum displacement of 0.89 mm—almost ninefold that of center welding. Such a marked difference underscores a pronounced increase in material flow during edge welding, corroborated by the sheet deformation observed in the welding simulation. This heightened deformation likely stems from the reduced volume of solid metal countering the electrode force in edge welding scenarios.

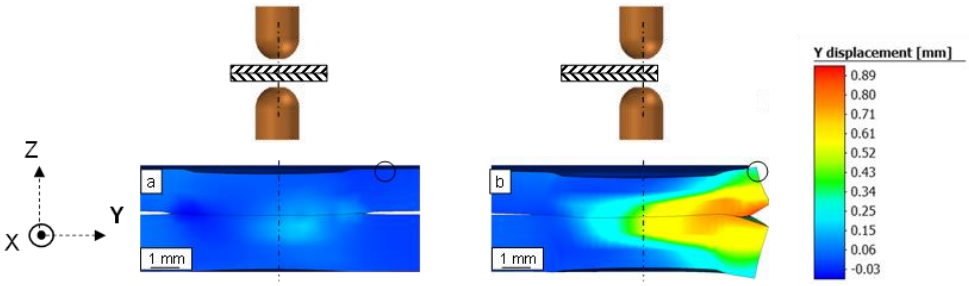

Figure 8. Y displacement (radial) shown for (**a**) a weld in the center of a sheet and for (**b**) edge welding. The circle marks a 4 mm radius from the spot weld's center, with the dashed line indicating the electrode position during welding.

The stress examination in Figure 4 can be further elaborated by considering the stress distribution across the cross−section. An investigation time of 140 ms, which coincides with the peak stress period, was selected before the onset of plastic deformation mitigates these stresses. As evident from Figure 9b, during edge welding, there is noticeable plastic displacement in the Y direction. This is driven by pronounced tensile stresses in the X direction. In contrast, center welding exhibits significantly reduced stresses in the X direction, leading to a smaller extent of radial displacement.

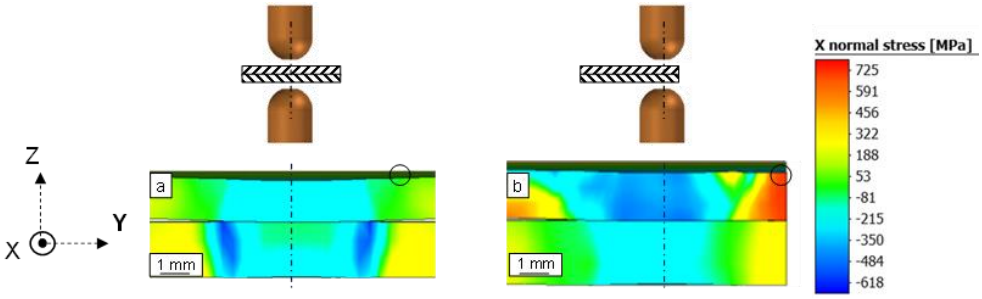

Figure 9. X normal stress (tangential) shown for (**a**) a weld in the center of a sheet and for (**b**) edge welding during the welding process at 140 ms. The circle marks a 4 mm radius from the spot weld's center, with the dashed line indicating the electrode position during welding.

Figure 10 depicts the change in tensile stress state due to material flow during the welding process at different locations. This is shown by plotting both the temperature and tensile stresses in the X direction (parallel to the sheet's edge) for both welding simulations. The orange box indicates the availability of liquid zinc, representing the period during which the surface temperature of the sheet exceeds the melting point of zinc at 420 °C.

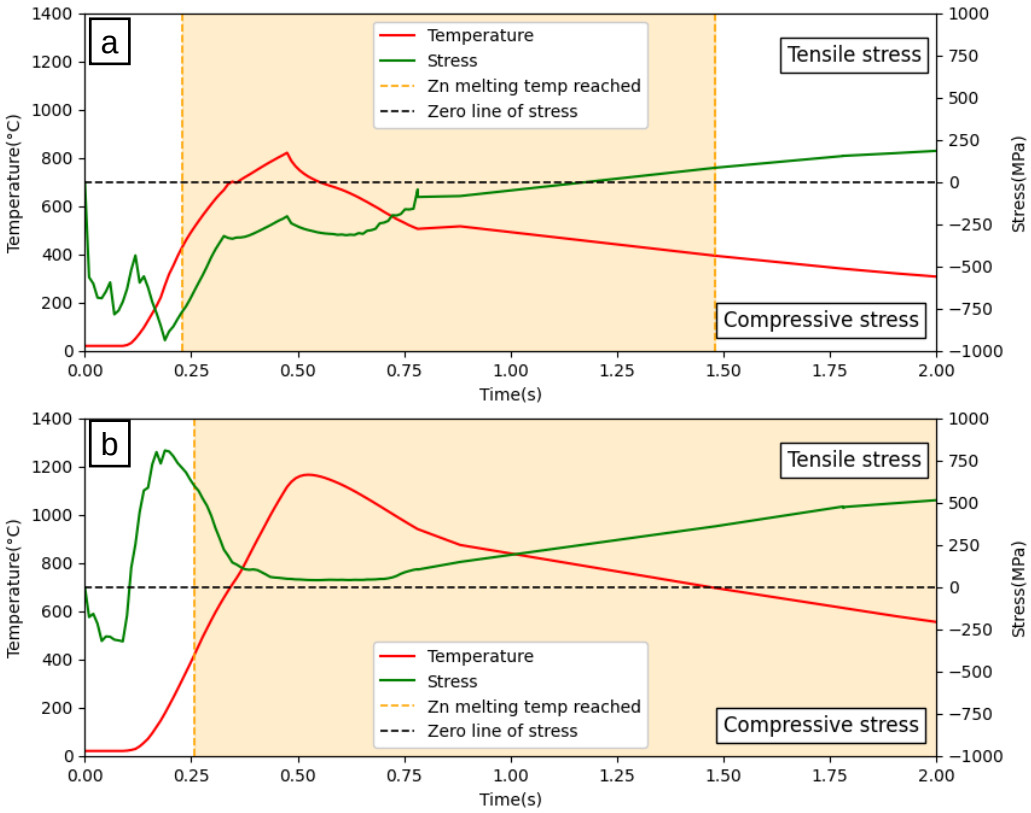

Figure 10. Comparison of stresses in X−direction and temperatures at the selected analysis points during (**a**) welding in the center of a sheet and (**b**) edge welding.

Regardless of the spot weld's position during the squeeze time, the stress at the analyzed area drops to a negative value, indicating a compressive load state due to the force applied by the electrode. When the spot weld is at the center, the compressive stress decreases once the welding current is initiated. In contrast, when the spot weld is at the sheet edge, during the same welding period, the stress rapidly transitions from approximately −500 MPa to a positive value, reaching around +800 MPa, indicating a transition to a tensile stress state. These differences are explained by the previously discussed phenomenon caused by geometric condition changes, causing material to flow outward at the sheet's edge and thus generating tensile stress at the deformation zone. By the 0.2 s mark of the welding process, the tensile stress of the edge welding case gradually decreases. This stress evolution is due to stress relief through plastic deformation as the temperature rises, bringing it down to a lower absolute value. During the cooling process, the stresses in both welding scenarios increase to a positive range (tensile stress) due to material expansion caused by heat transfer from the welding nugget to the material surface after the electrode cap leaves the welding position. Summarizing the above analysis, it is concluded that when welding at the edge, the observed location is subjected to tensile stress throughout the entire welding process, and its peak value is significantly higher than the tensile stress generated when welding at the center. Additionally, after 0.25 s, this tensile stress appears alongside the liquid zinc, combining known influence factors for LME formation.

The evidence to date confirms that this crack aligns with the fundamental conditions for LME cracks within the iron−zinc system. However, research by Nicholas and Bhattacharya suggest a more specific condition for LME occurrence during the RSW process: the tensile stress must surpass the material's yield strength [9,11]. Additionally, in hot tensile tests, Béal found LME occurrence only when the tensile stress marginally exceeded the yield stress [34]. Béal also termed this phenomenon as the "critical stress" essential for fostering LME at elevated temperatures. In line with these findings, Jung's finite element analysis demonstrated that the primary driver for heightened LME susceptibility is the tensile stress surpassing the yield strength [13].

When applying this LME judgement criterion, it is necessary to study the tensile stresses in relation to yield strength. Since yield strength is temperature−dependent, investigating the temperature distribution over time, as shown in Figure 10, is essential. Figure 10a depicts the highest peak temperature achieved during welding at the center of a sheet, which is around 800 °C, while Figure 10b shows that edge welding experiences higher peak temperatures, just below 1200 °C. There is also a slower temperature drop, as indicated by the larger orange box in Figure 10b, representing the duration when the temperature exceeds 420 °C. The higher peak temperature indicates that the yield stress is significantly lower, increasing susceptibility to plastic flow compared to center welding. This change in yield strength necessitates comparing not just the total tensile stresses but also analyzing how tensile stress relates to yield strength at elevated temperatures.

Using the known yield strengths at various temperatures, as provided by the material parameters in [32], a sixth−order polynomial can be derived to describe this behavior:

$$f(x) = 9.949e^{-15} \cdot x^6 - 4.503e^{-11} \cdot x^5 + 7.591e^{-8} \cdot x^4 - 5.665e^{-5} \cdot x^3 + 0.01672 \cdot x^2 - 1.826 \cdot x + 986 \quad (1)$$

In the simulation, the observed tensile stresses are compared to the temperature−dependent yield strength. This comparison is achieved by dividing the tensile stress by the yield strength, calculated for the specific temperatures occurring during the welding simulation. If the resulting value is equal to or greater than 1, it indicates plastic flow.

Figure 11 presents the outcome of this calculation. It shows the ratio of stress to yield strength, plotted against temperature for edge welding at the previously mentioned examination site. During the period when liquid zinc is present, the tensile stress at the chosen analysis point exceeds the DP1200 DH yield strength at two instances: 0.4 s and 0.7 s, indicative of plastic flow. Having met this final verification condition, the observed

cracking in this study's edge welding is identified as a novel category of LME crack specific to RSW.

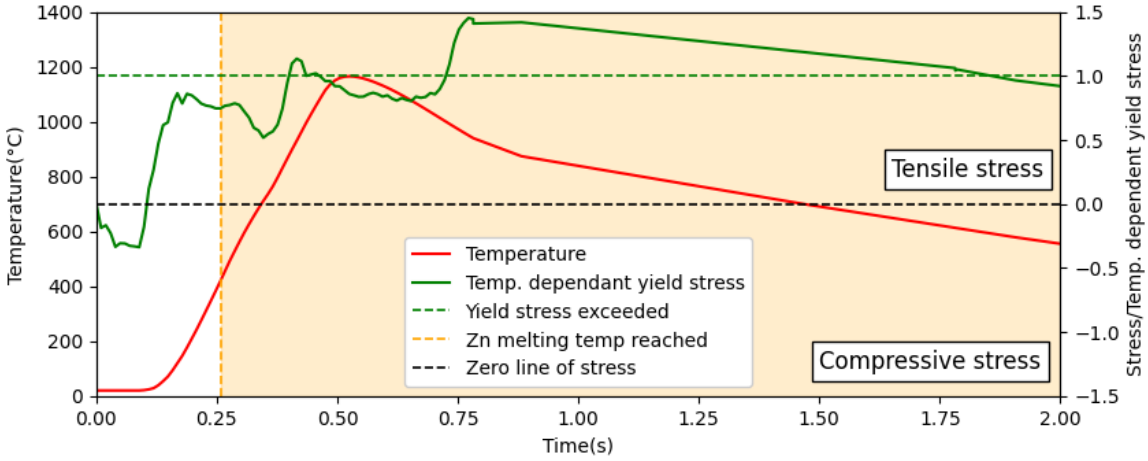

Figure 11. Investigation of occurring tensile stress standardized to the yield strength at the present temperatures for the edge welding.

5. Conclusions and Outlook

This study explored the DP1200 DH and mild steel stack−up cracking behavior in resistance spot welding under reduced flange width conditions. Through designed experiments, SEM and EDX analyses, and finite element simulation, the mechanism of this cracking behavior was analyzed, leading to the identification of a new type of LME crack. Based on the results revealed from this study, the following conclusions can be drawn:

1. When the stack−up explored in this study is spot−welded with a flange width less than or equal to 4 mm, severe edge cracking appears on the AHSS side. The crack radiates and points toward the edge of the sheet.
2. By examining the influence of the zinc coating on crack formation, it is known that the occurrence of the crack is due to the presence of the zinc coating, which determines that the crack does not belong to the category of mechanical cracks.
3. Based on the fracture mode and the penetration of liquid zinc, combined with the finite element analysis revealing the simultaneous occurrence of liquid zinc and tensile stress exceeding the yield strength of DP1200 DH, this has been identified as a new LME crack type in the RSW of galvanized AHSS.
4. Contrasting this with known LME cracks, the tensile stress prompting this new LME crack primarily arises from significant radial material deformation near the sheet's edge.
5. Preventing these LME cracks hinges on optimizing either welding parameters or boundary conditions to minimize tensile stress directed towards the sheet edge.

Author Contributions: Conceptualization, K.Y. and G.S.; methodology, K.Y.; validation, G.S.; formal analysis, K.Y.; investigation, M.B.; resources, M.R. and G.M.; data curation, K.Y. and G.S.; writing—original draft preparation, K.Y.; writing—review and editing, K.Y. and G.S.; visualization, G.S.; supervision, M.B., G.M. and M.R.; project administration, K.Y. and G.S.; funding acquisition, M.R. and G.M. All authors have read and agreed to the published version of the manuscript.

Funding: This research was funded by the German Federal Ministry of Economic Affairs and Climate Action through the German Federation of Industrial Research Associations (AiF) as part of the program for promoting industrial cooperative research (IGF) on the basis of a decision by the German Bundestag, grant number IGF 21483 BG. The APC was funded by Fraunhofer-Gesellschaft.

Data Availability Statement: Not applicable.

Acknowledgments: The research project 21483 BG/P 1488 "Validation of methods for the avoidance of Liquid Metal Embrittlement on Realistic Principle Components" from the Research Association for Steel Application (FOSTA), Düsseldorf, is supported by the Federal Ministry of Economic Affairs and Climate Action through the German Federation of Industrial Research Associations (AiF) as part of the program for promoting industrial cooperative research (IGF) on the basis of a decision by the German Bundestag. The project is carried out at LWF, Paderborn, IWF, Magdeburg and Fraunhofer IPK, Berlin.

Conflicts of Interest: The authors declare no conflict of interest.

References

1. Meschut, G.; Matzke, M.; Hoerhold, R.; Olfermann, T. Hybrid Technologies for Joining Ultra−high−strength Boron Steels with Aluminum Alloys for Lightweight Car Body Structures. *Procedia CIRP* **2014**, *23*, 19–23. [CrossRef]
2. Ma, Y.; Yu, Y.; Geng, P.; Ihara, R.; Maeda, K.; Suzuki, R.; Suga, T.; Ma, N. Fracture modeling of resistance spot welded ultra−high−strength steel considering the effect of liquid metal embrittlement crack. *Mater. Des.* **2021**, *210*, 110075. [CrossRef]
3. Jin, W.; Lalachan, A.; Murugan, S.P.; Ji, C.; Park, Y. Effect of Process Parameters and Nugget Growth Rate on Liquid Metal Embrittlement (LME) Cracking in the Resistance Spot Welding of Zinc−Coated Steels. *J. Weld. Join.* **2022**, *40*, 464–477. [CrossRef]
4. Jeon, W. −S.; Sharma, A.; Jung, J.P. Liquid Metal Embrittlement of Galvanized TRIP Steels in Resistance Spot Welding. *Metals* **2020**, *10*, 787. [CrossRef]
5. Mendala, J. Liquid metal embrittlement of steel with galvanized coatings. *IOP Conf. Ser. Mater. Sci. Eng.* **2012**, *35*, 012002. [CrossRef]
6. Zhou, L.; Zhang, T.; Zhang, Z.; Lei, Z.; Zhu, S. Monitoring of resistance spot welding expulsion based on machine learning. *Sci. Technol. Weld. Join.* **2022**, *27*, 292–300. [CrossRef]
7. Ling, Z.; Chen, T.; Wang, M.; Kong, L. Reducing liquid metal embrittlement cracking in resistance spot welding of Q&P980 steel. *Mater. Manuf. Process.* **2020**, *35*, 1392–1399. [CrossRef]
8. Ashiri, R.; Mostaan, H.; Park, Y. −D. A Phenomenological Study of Weld Discontinuities and Defects in Resistance Spot Welding of Advanced High Strength TRIP Steel. *Metall. Mater. Trans. A* **2018**, *49*, 6161–6172. [CrossRef]
9. Bhattacharya, D. Liquid metal embrittlement during resistance spot welding of Zn−coated high−strength steels. *Mater. Sci. Technol.* **2018**, *34*, 1809–1829. [CrossRef]
10. Bhattacharya, D.; Findley, K.; Ghassemi−Armaki, H.; Speer, J.; Aa, E.M. Quantitative assessment of the characteristics of liquid metal embrittlement during resistance spot welding of Zn−coated high−strength steels. In Proceedings of the Sheet Metal Welding Conference XVIII, Livonia, MI, USA, 17–18 October 2018; pp. 17–18.
11. Nicholas, M.G.; Old, C.F. Liquid metal embrittlement. *J. Mater. Sci.* **1979**, *14*, 1–18. [CrossRef]
12. DiGiovanni, C.; Shojaee, M.; Biro, E.; Zhou, N.Y. Effect of external loading on liquid metal embrittlement severity during resistance spot welding. *Manuf. Lett.* **2022**, *33*, 11–14. [CrossRef]
13. Jung, G.; Suh, D.W. *Zn−Assisted Liquid Metal Embrittlement of High Mn Austenitic Steels*; Pohang University of Science and Technology: Pohang, Republic of Korea, 2015.
14. El−Sari, B.; Biegler, M.; Rethmeier, M. Investigation of the LME Susceptibility of Dual Phase Steel with Different Zinc Coatings. *Metals* **2023**, *13*, 890. [CrossRef]
15. DiGiovanni, C.; Bag, S.; Mehling, C.; Choi, K.W.; Macwan, A.; Biro, E.; Zhou, N.Y. Reduction in liquid metal embrittlement cracking using weld current ramping. *Weld. World* **2019**, *63*, 1583–1591. [CrossRef]
16. Song, S.; Shojaee, M.; Midawi, A.; Sherepenko, O.; Ghassemi−Armaki, H.; Biro, E. Influence of Expulsion and Heat Extraction Resulting from Changes to Electrode Force on Liquid Metal Embrittlement during Resistance Spot Welding. *J. Mater. Res. Technol.* **2023**, *23*, 1458–1470. [CrossRef]
17. Lalachan, A.; Murugan, S.P.; Jin, W. −S.; Park, Y.−D. Liquid metal embrittlement in Zn−coated steel resistance spot welding: Critical electrode−contact and nugget growth for stress development and cracking. *J. Mater. Process. Technol.* **2023**, *318*, 118009. [CrossRef]
18. Böhne, C.; Meschut, G.; Biegler, M.; Frei, J.; Rethmeier, M. Prevention of liquid metal embrittlement cracks in resistance spot welds by adaption of electrode geometry. *Sci. Technol. Weld. Join.* **2020**, *25*, 303–310. [CrossRef]
19. Van Der Aa, E.; Rana, R. Optimization of Hot Forming Temperature to Minimize Liquid Metal Embrittlement Induced Cracking in Resistance Spot Welded Zinc-Coated Medium Manganese Steel. *Steel Res. Int.* **2023**, 2300045. [CrossRef]
20. Kim, J.U.; Murugan, S.P.; Kim, J.S.; Yook, W.; Lee, C.Y.; Ji, C.; Jeon, J.B.; Park, Y. −D. Liquid metal embrittlement during the resistance spot welding of galvannealed steels: Synergy of liquid Zn, α−Fe(Zn) and tensile stress. *Sci. Technol. Weld. Join.* **2021**, *26*, 196–204. [CrossRef]
21. Ghatei, A.; Khan, M.S.; Lee, M.; Zhou, Y. High−temperature phase evolution of the ZnAlMg coating and its effect on mitigating liquid−metal−embrittlement cracking. *Acta Mater.* **2022**, *229*, 117836. [CrossRef]
22. Wang, X.; Xie, Y.; Liu, Z.; Sun, Q.; Shen, X.; Zhang, Q.; Hu, Z.; Misra, R.D.K. Zn−induced liquid metal embrittlement and mechanical properties of advanced high−strength steel with resistance spot weld. *Mater. Sci. Eng. A* **2022**, *843*, 143088. [CrossRef]

23. Ellenrieder, G.; Gänsicke, T.; Sandiano, J.; Goede, M.; Herrmann, H.G. Die Leichtbaustrategien. In *Leichtbau in der Fahrzeugtechnik*; Friedrich, H.E., Ed.; In ATZ/MTZ−Fachbuch; Springer Fachmedien: Wiesbaden, Germany, 2017; pp. 45–123. [CrossRef]
24. Manzenreiter, T.; Faderl, J.; Szinyur, J. *Herausforderungen bei der Produktion und Verarbeitung von Presshärtendem Stahl Mit Kathodischem Korrosionsschutz. 20.*; Sondertagung Widerstandsschweißen: Duisburg, Germany, 2007.
25. Society, A.W.; Murugan, S.P.; Park, Y. −D.; Vijayan, V.; Ji, C. Four Types of LME Cracks in RSW of Zn−Coated AHSS. *Weld. J.* **2020**, *99*, 75s–92s. [CrossRef]
26. *DA 239-100:2016*; Sheet Steel for Cold Forming. National Standard. Verband der Automobilindustrie e.V. (VDA): Berlin, Germany, 2016.
27. Voestalpine Stahl GmbH. Dual-Phase High-Ductility Steels. EN-12062019 Datasheet, June 2019.
28. Voestalpine Stahl GmbH. Mild Steels. EN-09082019 Datasheet, October 2022.
29. Benlatreche, Y.; Dupuy, T.; Mescolini, D. Design rules to minimize LME (Liquid Metal Embrittlement). In Proceedings of the Joining in Car Body Engineering, Bad Nauheim, Germany, 9–11 April 2019.
30. *ISO 5821:2010*; Resistance Welding—Spot Welding Electrode Caps (German Version). Deutsches Institut für Normung (DIN): Berlin, Germany; Beuth: Berlin, Germany, 2010.
31. *SEP 1220−2:2011*; Testing and Documentation Guideline for the Joinability of Thin Sheets of Steelpart 2: Resistance Spot Welding. Stahlinstitut VDEh: Berlin, Germany; Beuth: Berlin, Germany, 2011.
32. Frei, J.; Biegler, M.; Rethmeier, M.; Böhne, C.; Meschut, G. Investigation of liquid metal embrittlement of dual phase steel joints by electro−thermomechanical spot−welding simulation. *Sci. Technol. Weld. Join.* **2019**, *90*, 624–633. [CrossRef]
33. *ISO/TS 18166:2016*; Numerical Welding Simulation—Execution and Documentation (German Version). Deutsches Institut für Normung: Berlin, Germany; Beuth: Berlin, Germany, 2016.
34. Beal, C. Mechanical Behaviour of a New Automotive High Manganese TWIP Steel in the Presence of Liquid Zinc. Doctoral Dissertation, Intelligence and National Security Alliance, Lyon, France, 2011.